Nondissipative simulation methods for collisionless electrostatic plasmas [1]

Tomo-Hiko Watanabe[2]
National Institute for Fusion Science / The Graduate University for Advanced Studies, Toki, Gifu, 509-5292, Japan

October 11, 2003

[1]This document is prepared as a lecture note for Autumn College on Plasma Physics: Long-Lived Structures and Self Organization in Plasmas at International Centre for Theoretical Physics, Trieste, Italy. All of our works described here are based on collaborations with Dr.H.Sugama (NIFS).

[2]*E-mail:* tomo@nifs.ac.jp

Contents

Chapter 1

Introduction

According to the development of computer technologies, numerical simulations of plasma dynamics have rapidly grown as a powerful tool for studies of various nonlinear phenomena in fusion, astrophysical, and laboratory plasmas. In the field of the magnetic confinement fusion, for example, the anomalous transport studies based on the computer simulation have been very actively promoted in the last decade. A collisionless micro-scale turbulence is one of the key issues in the anomalous transport research, where one needs to taken into account the kinetic effects. However, there are various difficulties in simulations of the collisionless plasma dynamics even with the electrostatic approximation. A main purpose of this lecture is to explain methods of the collisionless plasma simulations, and to provide an opportunity for considering their importance.

Generally speaking, a simulation study consists of several steps. The first step is to find governing equations which are applied to a physical phenomena being interested in. The second is to consider a numerical method employed for finding an approximate solution of the governing equations. Implementation and execution of the simulation code are included in the third step. After obtaining the results, finally, one can go to the step for studying the phenomena reproduced by the numerical simulation. Although many physicists seem to pay more attention to the first and the last steps than the others, the second step is also indispensable and important to obtaining a correct result. If an inadequate method is employed, all of the efforts in the other steps may come to nothing.

Numerical simulation methods for the Vlasov-Possion and the collisionless drift kinetic systems are discussed in the latter part of this lecture. Since both of the kinetic equations for the one-body velocity distribution f can be represented as

$$\frac{\partial f}{\partial t} = -\{f, H\} \tag{1.1}$$

by using the Hamiltonian H and the Possion brackets $\{,\}$, it is considered that numerical methods suitable for collisionless plasma simulations is related to that for a Hamiltonian system. Thus, let us first learn numerical integration schemes suitable for the Hamiltonian system with a small number of variables, where we discuss the symplectic numerical integration method which provides a basis of the nondissipative simulation schemes for

the Vlasov and the collisionless drift kinetic equations. One will find a close relationship between the numerical method and the classical mechanics. Benchmark tests of simulations shown in the lecture are made for problems of a nonlinear oscillator (described by the Jacobi elliptic functions) and the plasma echo. The results are useful to check whether the time-reversibility and the phase mixing process intrinsic to the collisionless plasmas are correctly simulated or not. Finally, the closure problem in kinetic-fluid models will also be briefly discussed.

Chapter 2

Numerical Scheme for the Hamiltonian system

Before going to investigate simulation methods for the collisionless plasmas with *infinite* degrees of freedom, it is instructive to learn numerical approaches to Hamiltonian systems with a small number of variables. Since all of the examples shown here has analytical solutions, it will be able to check accuracy and efficiency of numerical schemes and their limitations.

2.1 Basic schemes

2.1.1 Harmonic oscillator

One of the simplest examples of the Hamiltonian system is the harmonic oscillator,

$$\frac{d^2x}{dt^2} \equiv \ddot{x} = -x \ , \tag{2.1}$$

which is also represented as

$$\begin{cases} dq/dt \equiv \dot{q} = \partial H(q,p)/\partial p \\ dp/dt \equiv \dot{p} = -\partial H(q,p)/\partial q \end{cases} \qquad \text{with} \quad H(q,p) = \frac{1}{2}\left(p^2 + q^2\right) \ . \tag{2.2}$$

In this section, let us consider a numerical solver for Eq.(2.1) or (2.2) with the initial condition of $x(t=0) = q(t=0) = 1$ and $v(t=0) = p(t=0) = 0$. The analytical solution is trivial,

$$q(t) = \cos t \ , \qquad p(t) = -\sin t \ . \tag{2.3}$$

Eq.(2.2) is more suitable for the numerical time-integration than Eq.(2.1), since it contains only the first derivative for the time variable t.

Whenever we numerically solve equations as an initial-value problem, we need to discretize the time variable t with finite spacing Δt (that is assumed to be constant

hereafter). A mapping generated by the harmonic oscillator in Eq.(2.3) for a discretized time step from $t = t^n \equiv n\Delta t$ to $t = t^{n+1} \equiv (n+1)\Delta t$ is given by

$$\begin{pmatrix} q^{n+1} \\ p^{n+1} \end{pmatrix} = \begin{pmatrix} \cos\Delta t & \sin\Delta t \\ -\sin\Delta t & \cos\Delta t \end{pmatrix} \begin{pmatrix} q^n \\ p^n \end{pmatrix} \tag{2.4}$$

$$\equiv \mathsf{M}_H \begin{pmatrix} q^n \\ p^n \end{pmatrix} , \tag{2.5}$$

where the super scripts denote the time step number.

2.1.2 Conventional approach

Forward Euler method The most primitive numerical integration method of the ordinary differential equation (O.D.E.) is the forward (explicit) Euler methods,

$$\begin{cases} q^{n+1} = q^n + \Delta t p^n \\ p^{n+1} = p^n - \Delta t q^n \end{cases} , \tag{2.6}$$

where only the variables at $t = t^n$ are employed in calculation of the right-hand side (r.h.s.) of the O.D.E's. An important property of the forward Euler method can be analyzed by substituting $q(t) = q_0 \exp(i\omega t)$ and $p(t) = p_0 \exp(i\omega t)$ into Eq.(2.6). Then, one finds a complex amplification factor of q (or p) within a time step, $g \equiv \exp(i\omega\Delta t)$. It is straightforward to obtain

$$g = 1 \pm i\Delta t = \sqrt{1+\Delta t^2} e^{\pm i\theta} \quad \text{for} \quad \theta = \tan^{-1}\Delta t \ . \tag{2.7}$$

Since $|g| > 1$ for any $\Delta t > 0$, the forward Euler method is *unstable* when it is applied to the harmonic oscillator. It means that the oscillation amplitude as well as the total energy monotonically grows in time. The numerical solution, then, has a spiral orbit in the (q, p)-phase space as is seen in Fig.2.1 (a). In the Taylor expansion of $|g|$, the leading order term in difference from the analytical solution in Eq.(2.3) is proportional to Δt. Then, the forward Euler method is a first-order scheme.

Backward Euler method Similar to Eq.(2.6), the backward Euler scheme is given by

$$\begin{cases} q^{n+1} = q^n + \Delta t p^{n+1} \\ p^{n+1} = p^n - \Delta t q^{n+1} \end{cases} . \tag{2.8}$$

Equivalently,

$$\begin{pmatrix} q^{n+1} \\ p^{n+1} \end{pmatrix} = \frac{1}{1+\Delta t^2} \begin{pmatrix} 1 & \Delta t \\ -\Delta t & 1 \end{pmatrix} \begin{pmatrix} q^n \\ p^n \end{pmatrix} . \tag{2.9}$$

This is an implicit time integrator, since both q^{n+1} and p^{n+1} are used on the r.h.s. of Eq.(2.8). Using the same procedure as given above, one finds

$$g = \frac{1}{1 \pm i\Delta t} = \frac{1}{\sqrt{1+\Delta t^2}} e^{\pm i\theta} \quad \text{for} \quad \theta = \tan^{-1}\Delta t \ . \tag{2.10}$$

Contrary to the previous case, $|g| < 1$ for any $\Delta t > 0$ in the backward Euler method. Thus, the oscillation amplitude as well as the total energy monotonically decreases in time as is seen in Fig.2.1 (b). Therefore, the backward Euler scheme turns out to be *stable* and involves numerical dissipation. This is also the first-order scheme.

Remedies Generally speaking, stable methods are more preferable than unstable ones in actual applications, since one can continue numerical calculations no matter how dissipative the employed scheme is. If one uses a higher-order scheme, such as the Runge-Kutta method that is widely used in numerical integration of O.D.E.'s, the numerical error could be suppressed in a small level. Such approach is effective if the numerical dissipation is negligibly smaller than the real dissipation contained in the governing equations. The dissipative integrator, however, breaks the conservation properties of the Hamilton system.

There is a very simple remedy for the numerical dissipation in solving Eq.(2.2). Combining the above two Euler methods, one may try to use

$$\begin{cases} q^{n+1} = q^n + \Delta t p^n \\ p^{n+1} = p^n - \Delta t q^{n+1} \end{cases} . \tag{2.11}$$

This is an explicit method, since, in order to obtain p^{n+1}, one can use q^{n+1} that is calculated only from q^n and p^n. By a similar analysis in the above, one finds

$$\left(e^{i\omega\Delta t/2} - e^{-i\omega\Delta t/2}\right)^2 = -\Delta t^2 . \tag{2.12}$$

If $\Delta t \leq 2$, then ω is real-valued, $\omega\Delta t/2 = \pm\sin^{-1}(\Delta t/2)$. This means that the scheme is *marginally stable*, $|g| = 1$, for $\Delta t < 2$. It is also straightforward to find an invariant

$$\frac{1}{2}\left(p^2 + q^2\right) + \frac{\Delta t}{2} qp = \text{const.} , \tag{2.13}$$

while the energy $(p^2 + q^2)/2$ is not conserved but oscillates around a constant level (with no secular increase nor decrease). Then, the trajectory in the (q, p)-phase space is given by a closed elliptic orbit as is shown in Fig.2.1 (c).

2.2 Symplectic approach

2.2.1 First-order method

Why can the integration method given in Eq.(2.11) work so well in calculation of the Harmonic oscillator? Is it also effective to other Hamiltonian systems? Answers to these questions would be found by considering the properties of the Hamiltonian system.

Let us remember the canonical equation of Hamilton represented by the symplectic formulation, [1]

$$\dot{\boldsymbol{\eta}} = \mathsf{J}\frac{\partial H}{\partial \boldsymbol{\eta}} , \tag{2.14}$$

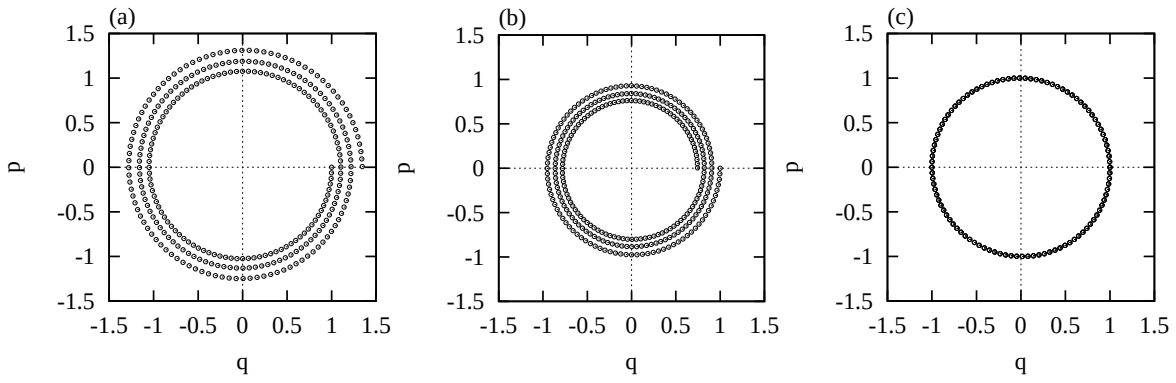

Figure 2.1: Numerical simulation results of the harmonic oscillator obtained by (a) the forward Euler, (b) the backward Euler, and (c) the symplectic methods. The simulations are run up to $t = 6\pi$ with $\Delta t = \pi/100$.

where

$$\boldsymbol{\eta} = \begin{pmatrix} \boldsymbol{q} \\ \boldsymbol{p} \end{pmatrix} \quad \text{and} \quad \mathsf{J} = \begin{pmatrix} \mathsf{O} & \mathsf{I} \\ -\mathsf{I} & \mathsf{O} \end{pmatrix} . \tag{2.15}$$

O and I denote the zero and unit matrices, respectively. Consider a coordinate transform from $\boldsymbol{\eta}$ to $\boldsymbol{\zeta}$ given by the Jacobian matrix M,

$$M_{ij} = \frac{\partial \zeta_i}{\partial \eta_i} . \tag{2.16}$$

Then, Eq.(2.14) is transformed as

$$\dot{\boldsymbol{\zeta}} = \mathsf{M}\mathsf{J}\tilde{\mathsf{M}}\frac{\partial H}{\partial \boldsymbol{\zeta}} , \tag{2.17}$$

where $\tilde{\mathsf{M}}$ means the transposed matrix of M. If the symplectic condition

$$\mathsf{M}\mathsf{J}\tilde{\mathsf{M}} = \mathsf{J} \tag{2.18}$$

is satisfied, the transformation from $\boldsymbol{\eta}$ to $\boldsymbol{\zeta}$ is canonical.

The matrix denoted by M_H in Eq.(2.4) satisfies the symplectic condition, Eq.(2.18), since the solution of the Hamilton's equation generates the canonical transform. It is also trivial that $\det \mathsf{M}_H = 1$. Now, rewriting Eq.(2.11) to

$$\begin{pmatrix} q^{n+1} \\ p^{n+1} \end{pmatrix} = \begin{pmatrix} 1 & \Delta t \\ -\Delta t & 1 - \Delta t^2 \end{pmatrix} \begin{pmatrix} q^n \\ p^n \end{pmatrix} \tag{2.19}$$

$$\equiv \mathsf{M}_S \begin{pmatrix} q^n \\ p^n \end{pmatrix} . \tag{2.20}$$

then, one can easily confirm $\det \mathsf{M}_S = 1$ and $\mathsf{M}_S\mathsf{J}\tilde{\mathsf{M}}_S = \mathsf{J}$. It means that that a mapping of (q^n, p^n) to (q^{n+1}, p^{n+1}) given in Eq.(2.11) is a symplectic (canonical) transform. This is why the numerical integration scheme in Eq.(2.11) is called a symplectic integrator.

The first-order symplectic integrator in Eq.(2.11) can also be applied to a separable Hamiltonian system with $H(q,p) = T(p) + V(q)$,

$$\left\{ \begin{array}{l} q^{n+1} = q^n + \Delta t(\partial T/\partial p)_{p=p^n} \\ p^{n+1} = p^n - \Delta t(\partial V/\partial q)_{q=q^{n+1}} \end{array} \right. . \tag{2.21}$$

Rewriting Eq.(2.21) into a matrix form,

$$\left(\begin{array}{c} q^{n+1} \\ p^{n+1} \end{array} \right) = \left(\begin{array}{cc} 1 & 0 \\ B & 1 \end{array} \right) \left(\begin{array}{cc} 1 & A \\ 0 & 1 \end{array} \right) \left(\begin{array}{c} q^n \\ p^n \end{array} \right) \tag{2.22}$$

$$\equiv \mathsf{M}_B \mathsf{M}_A \left(\begin{array}{c} q^n \\ p^n \end{array} \right) \tag{2.23}$$

$$\equiv \mathsf{M}_{AB} \left(\begin{array}{c} q^n \\ p^n \end{array} \right) , \tag{2.24}$$

where $A = \Delta t(\partial T/\partial p)_{p=p^n}/p^n$ and $B = -\Delta t(\partial V/\partial q)_{q=q^{n+1}}/q^{n+1}$. For any A and B, one finds that M_{AB} and M_A as well as M_B satisfy the symplectic condition, and that $\det \mathsf{M}_{AB} = \det \mathsf{M}_A = \det \mathsf{M}_B = 1$. This is because M_A as well as M_B represents a generalized *free motion* in the phase space (namely, the trajectory is parallel to the q or p axis), and thus, generates the canonical transform. Since successive operations of canonical transforms is also canonical in total, M_{AB} satisfies the symplectic condition.

2.2.2 Higher-order methods

Using the notation of $z = (q,p)$, the canonical equation with the separable Hamiltonian $H(q,p) = T(p) + V(q)$ can be represented as

$$\dot{z} = \{z, H(z)\} \equiv (D_T + D_V) z , \tag{2.25}$$

where operators D_T and D_V are defined as $D_T \equiv \{\ , T\}$ and $D_V \equiv \{\ , V\}$, respectively. Then, a formal solution of Eq.(2.25) from $t = t^n$ to t^{n+1} is written as

$$z^{n+1} = \exp[\int dt (D_T + D_V)] z^n , \tag{2.26}$$

which can be approximated by

$$z^{n+1} = \prod_{i=1}^{k} \exp(c_i \Delta t D_T) \exp(d_i \Delta t D_V) z^n + \mathcal{O}(\Delta t^{k+1}) . \tag{2.27}$$

Thus, one obtains the k-th order symplectic integrator, [2]

$$\prod_{i=1}^{k} \left\{ \begin{array}{l} q_i = q_{i-1} + c_i \Delta t(\partial T/\partial p)_{p=p_{i-1}} \\ p_i = p_{i-1} - d_i \Delta t(\partial V/\partial q)_{q=q_i} \end{array} \right. , \tag{2.28}$$

for $i = 1$ to k with $(q_0, p_0) = (q^n, p^n) = z^n$ and $(q_k, p_k) = (q^{n+1}, p^{n+1}) = z^{n+1}$. The transformation from z^n to z^{n+1} is symplectic, since it is a product of each symplectic mapping for the *free motion*.

For the first-order ($k = 1$), one finds $c_1 = d_1 = 1$, which leads to Eq.(2.11). The second-order scheme can also be obtained by expanding the r.h.s of Eqs.(2.26) and (2.27) and comparing the coefficients up to the second-order terms. The result of $c_1 = c_2 = 1/2$, $d_1 = 1$, and $d_2 = 0$ constructs the following mapping,

$$\left\{ \begin{array}{l} q^{n+1/2} = q^n + (\Delta t/2)(\partial T/\partial p)_{p=p^n} \\ p^{n+1} = p^n - \Delta t(\partial V/\partial q)_{q=q^{n+1/2}} \\ q^{n+1} = q^{n+1/2} + (\Delta t/2)(\partial T/\partial p)_{p=p^{n+1}} \end{array} \right. . \tag{2.29}$$

This is equivalent to the leap-frog integrator,

$$\left\{ \begin{array}{l} q^{n+1/2} = q^{n-1/2} + \Delta t(\partial T/\partial p)_{p=p^n} \\ p^{n+1} = p^n - \Delta t(\partial V/\partial q)_{q=q^{n+1/2}} \end{array} \right. , \tag{2.30}$$

which is widely used in particle-in-cell (P.I.C.) simulations [3].

The fourth-order integrator $S_4(\Delta t)$ has been obtained by Forest and Ruth [4] such that

$$\begin{aligned} c_1 = c_4 &= \frac{1}{2(2 - 2^{1/3})} , \quad c_2 = c_3 = \frac{1 - 2^{1/3}}{2(2 - 2^{1/3})} , \\ d_1 = d_3 &= \frac{1}{2 - 2^{1/3}} , \quad d_2 = -\frac{2^{1/3}}{2 - 2^{1/3}} , \quad d_4 = 0 . \end{aligned} \tag{2.31}$$

It is also known that S_4 is represented by successive operations of the second-order one, $S_2(\Delta t)$, [2]

$$S_4(\Delta t) = S_2(d_1 \Delta t) S_2(d_2 \Delta t) S_2(d_1 \Delta t) . \tag{2.32}$$

2.3 Non-separable Hamiltonian system

2.3.1 Implicit method

In the previous section, we have considered a separable Hamiltonian system with $H(q, p) = T(q) + V(q)$. However, no explicit integrator is known for a general type of the Hamiltonian. Then, let us consider an implicit scheme. The implicit midpoint rule,

$$\boldsymbol{U}^{n+1} = \boldsymbol{U}^n + \Delta t \boldsymbol{F}(\bar{\boldsymbol{U}}) \quad \text{with} \quad \bar{\boldsymbol{U}} = (\boldsymbol{U}^{n+1} + \boldsymbol{U}^n)/2 . \tag{2.33}$$

is the second-order method which can be applied to O.D.E.'s of $d\boldsymbol{U}/dt = \boldsymbol{F}(\boldsymbol{U})$. If we employ Eq.(2.33) for integrating the canonical equation of Hamilton with $H(q, p)$,

$$\left(\begin{array}{c} q^{n+1} \\ p^{n+1} \end{array} \right) = \left(\begin{array}{c} q^n \\ p^n \end{array} \right) + \Delta t \left(\begin{array}{c} \partial H/\partial p|_{\bar{q},\bar{p}} \\ -\partial H/\partial q|_{\bar{q},\bar{p}} \end{array} \right) , \tag{2.34}$$

where $\bar{q} = (q^n + q^{n+1})/2$ and $\bar{p} = (p^n + p^{n+1})/2$. Let us see that the mapping $(q^n, p^n) \to (q^{n+1}, p^{n+1})$ in Eq.(2.34) is a canonical transform [5]. Consider a generating function of the third kind, $G(q^{n+1}, p^n)$, that defines a canonical transform [1]

$$\begin{cases} q^n = -\partial G/\partial p^n \\ p^{n+1} = -\partial G/\partial q^{n+1} \end{cases} . \tag{2.35}$$

Substituting

$$G(q^{n+1}, p^n) = -q^{n+1}p^n + \Delta t H(\bar{q}, \bar{p}) + \frac{1}{2}\Delta t^2 H_q(\bar{q}, \bar{p}) H_p(\bar{q}, \bar{p}) \tag{2.36}$$

into Eq.(2.35), one finds

$$\begin{aligned} q^n &= q^{n+1} - \Delta t H_q \frac{\partial \bar{q}}{\partial p^n} - \Delta t H_p \frac{\partial \bar{p}}{\partial p^n} - \frac{1}{2}\Delta t^2 \frac{\partial}{\partial p^n}\left[H_q(\bar{q}, \bar{p}) H_p(\bar{q}, \bar{p})\right] , \\ p^{n+1} &= p^n - \Delta t H_q \frac{\partial \bar{q}}{\partial q^{n+1}} - \Delta t H_p \frac{\partial \bar{p}}{\partial q^{n+1}} - \frac{1}{2}\Delta t^2 \frac{\partial}{\partial q^{n+1}}\left[H_q(\bar{q}, \bar{p}) H_p(\bar{q}, \bar{p})\right] , \end{aligned}$$

where $H_q = \partial H/\partial q|_{\bar{q},\bar{p}}$ and $H_p = \partial H/\partial p|_{\bar{q},\bar{p}}$. If we define

$$\begin{cases} \bar{q} = q^{n+1} - (\Delta t/2) H_p(\bar{q}, \bar{p}) \\ \bar{p} = p^n - (\Delta t/2) H_q(\bar{q}, \bar{p}) \end{cases} , \tag{2.37}$$

one finds that Eq.(2.35) reduces to Eq.(2.34), namely, Eq.(2.34) is a canonical transform generated by $G(q^{n+1}, p^n)$.

2.3.2 Higher-order methods

Extension of Eq.(2.34) to the 4th-order method is straightforward by using the same successive operations as in Eq.(2.32),

$$S_4(\Delta t) = S_2(d_1\Delta t) S_2(d_2\Delta t) S_2(d_1\Delta t) .$$

The higher-order methods can be constructed in a similar way to Eq.(2.32).

2.4 Application to 3-mode equations

In this section, let us consider the following set of ordinary differential equations (so-called 3-mode equations in literatures of the drift wave turbulence),

$$\begin{cases} \dot{a} = b \\ \dot{b} = a - \delta a c \\ \dot{c} = 2\delta a b \end{cases} . \tag{2.38}$$

The above equations can be obtained by keeping only $(\pm 1, \pm 1)$ and $(0, \pm 2)$ modes in the continuity and vorticity equations for the Rayleigh-Taylor (interchange) instability while

truncating the higher modes. In section 4.2.2, the same equations are also derived from the drift kinetic equations for the ion temperature gradient (ITG) driven instability [6]. It is easy to confirm that Eq.(2.38) has two independent conserved quantities, such that

$$c - \delta a^2 = D_1 \tag{2.39}$$

$$b^2 + \frac{1}{2}c^2 - \frac{1}{\delta}c = D_2 \ . \tag{2.40}$$

Then, Eq.(2.38) is integrable, and its analytical solution is given by the Jacobi elliptic functions (see, for example, Ref.[6]). By substituting Eq.(2.39) into the second equation of Eq.(2.38) to eliminate c, one also finds that Eq.(2.38) reduces to the canonical equation for a and b with a separable Hamiltonian

$$H(a,b) = \frac{1}{2}b^2 + \frac{1}{2}(\delta D_1 - 1)a^2 + \frac{1}{4}\delta^2 a^4 \ , \tag{2.41}$$

that is,

$$\begin{cases} \dot{a} = \partial H(a,b)/\partial b = b \\ \dot{b} = -\partial H(a,b)/\partial a = (1-\delta D_1)a - \delta^2 a^3 \end{cases} \ . \tag{2.42}$$

A benefit of the implicit midpoint rule in Eq.(2.33) is applicability to a general form of O.D.E., such that $d\boldsymbol{U}/dt = \boldsymbol{F}(\boldsymbol{U})$. One can directly apply Eq.(2.33) to Eq.(2.38) by setting $\boldsymbol{U} = (a, b, c)$. On the other hand, the explicit symplectic integrator can also be used for integrating Eq.(2.42), since the Hamiltonian $H(a, b)$ is separable for a and b. Results of the numerical time integration is given in Fig.2.2, where three different methods are compared; the leap-frog integrator, the implicit midpoint rule, and the Runge-Kutta method. One can clearly see that the first two methods successfully reproduce the periodic solution of the 3-mode equations, while the Runge-Kutta scheme fails in spite of its higher-order accuracy than the others.

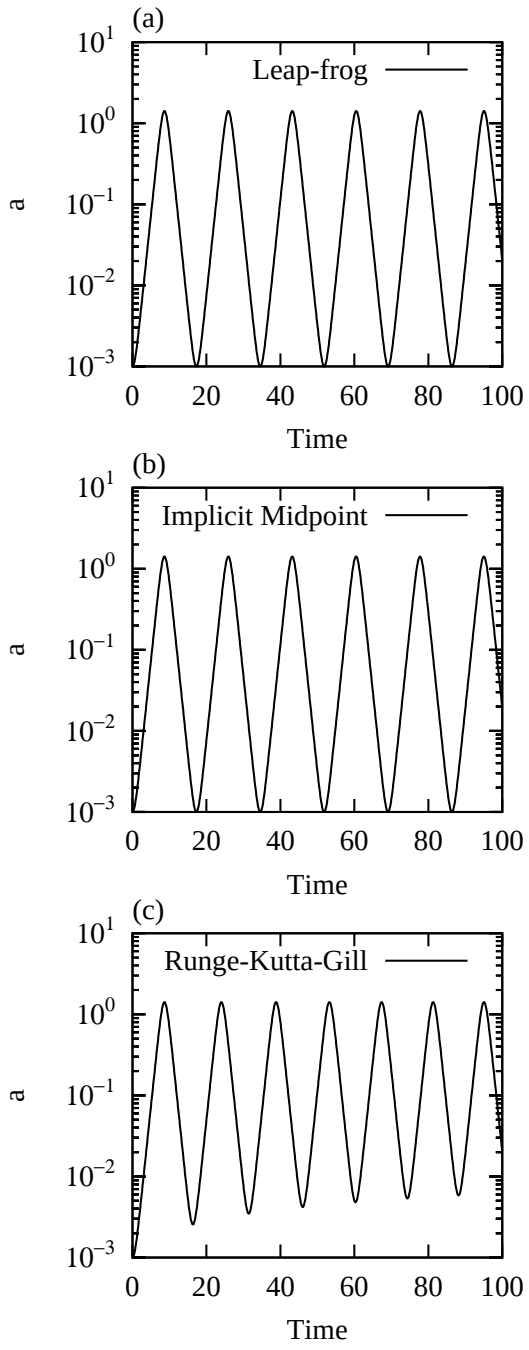

Figure 2.2: Time evolutions of a in the 3-mode equations obtained by (a) the leap-frog integrator, (b) implicit midpoint rule, and (c) the 4th-order Runge-Kutta method.

Chapter 3

Numerical simulation of the Vlasov-Possion system

In this chapter, we consider numerical simulation methods for the one-dimensional Vlasov-Poisson system,

$$\frac{\partial f}{\partial t} + v\frac{\partial f}{\partial x} + \frac{\partial \phi}{\partial x}\frac{\partial f}{\partial v} = 0 \ , \tag{3.1}$$

$$-\frac{\partial^2 \phi}{\partial x^2} = 1 - \int f dv \ , \tag{3.2}$$

where $f = f(x, v; t)$ is the one-body velocity distribution function of electrons. Background immobile ions are assumed. As is well known, since f is a constant of motion, Eq.(3.1) is represented as,

$$\frac{\partial f}{\partial t} = -\{f, H\} \tag{3.3}$$

for the conjugate pair of the coordinates, (x, v), where the Hamiltonian $H(x, v) = v^2/2 + \phi(x)$. While f is constant along the particle motion, it is stretched and folded by the Hamiltonian flow (particle trajectories) in the phase space. Then, fine-scale structures of f are generated in the phase space, while fluid variables given by velocity-space integrals are damped. This is known as the *phase mixing*.

3.1 Phase mixing

The phase mixing causes a severe problem in numerical simulations of collisionless kinetic plasmas (Vlasov, drift kinetic, gyrokinetic *etc.*). Historically, this point has been more clearly recognized in the Vlasov simulation rather than P.I.C. Let us see the difficulty in simulation of the Vlasov equation by considering a case of the neutral gas with no electric field ($\phi = 0$). Under the periodic boundary condition for x, an analytical solution of Eq.(3.1) with $\phi = 0$ is given by

$$f(x, v; t) = \sum_k f(k, v; t = 0) \exp(ikx - ikvt) \ , \tag{3.4}$$

where $f(k, v; t = 0)$ is a Fourier component of the initial condition $f(x, v; t = 0)$. k denotes the wave number. A scale-length of f along the v-axis becomes smaller with the time t, which is related to the *ballistic* motion of particles. In a case with a monotonic perturbation, $f(x, v; t = 0) = 1 + f_0(v) \cos kx$, the solution is given by

$$f(x, v; t) = f_0(v)[1 + \cos(kx - kvt)] \ . \tag{3.5}$$

For the Maxwellian initial distribution, $f_0(v) = \exp(-v^2/2)/\sqrt{2\pi}$, one finds that the density perturbation monotonically decays in time, $n(x; t) = \exp(-k^2t^2/2) \cos kx$.

Now, let us consider what happens in numerical simulations with finite resolution Δv in the velocity space. In the discretized velocity space, $v = j\Delta v$ (j is integer), Eq.(3.5) is represented as

$$f(x, j; t) = f_0(j\Delta v)[1 + \cos(kx - kj\Delta vt)] \ . \tag{3.6}$$

It is applicable not only to the Vlasov simulation but also to the (δf) P.I.C. method, since f can be dealt with only at a finite number of particle positions. At glance, one will find that Eq.(3.6) is periodic in t. At every $t = 2\pi/k\Delta v$, $f(x, j; t)$ returns to its original form, $f(x, j; t = 0)$, which is called *recurrence* [7]. Schematic plots of the recurrence are shown in Fig.3.1 for the case with $f_0(v) = \text{const}$. This is an artificial effect due to the insufficient resolution for the velocity space, and is similar to the *aliasing* error that may arise in discretization of continuous data. Thus, numerical simulation of this system is valid only for $t < t_r/2 = \pi/k\Delta v$ (t_r is called the recurrence time).

In a case with finite electric field [$\phi \neq 0$ given by Eq.(3.2)], the phase mixing process is much more complicated, since Eq.(3.1) contains a nonlinear term. A nonuniform electric field leads to inhomogeneous acceleration of particles depending on their positions, and generates fine-scale fluctuations of f in the real x-space as well, which is also regarded as a nonlinear mode coupling through the electric field.

3.2 Vlasov simulation method with symplectic integrator

Keeping the above discussion in mind, let us consider the Vlasov simulation method which directly solves Eq.(3.1) as a partial differential equation in the (x, v)-phase space. In 1970's, Cheng and Knorr proposed the splitting scheme which consists of three successive transforms of f [7],

$$\begin{cases} f^*(x, v) = f^n(x - v\Delta t/2, v) \\ f^{**}(x, v) = f^*(x, v - \Delta t \partial\phi/\partial x) \\ f^{n+1}(x, v) = f^{**}(x - v\Delta t/2, v) \end{cases} \ . \tag{3.7}$$

Since numerical simulations are carried out with finite resolution, an interpolation method is necessary to evaluate f at the position referred in the transformations. Here, we have used the Fourier series expansion in applications given below, while the cubic splines interpolation [8] is also widely employed. The coordinate transformation of $x - v\Delta t/2$ can be accurately calculated in the Fourier space by multiplying a phase shifting factor of

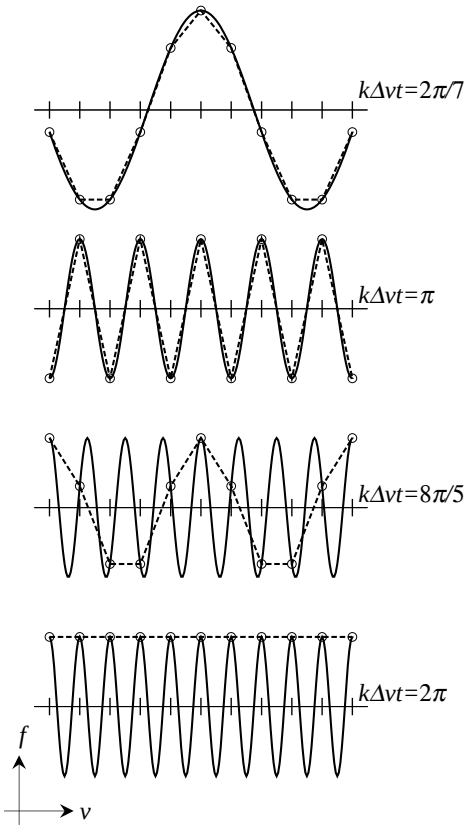

Figure 3.1: Schematic view of recurrence of the initial condition due to discretization of the velocity space.

$\exp(-ikv\Delta t/2)$. Similarly, the transformation of $v-\Delta t\partial\phi/\partial x$ is carried out in the velocity wave number space by multiplying $\exp(-i\ell\Delta t\partial\phi/\partial x)$. Here, ℓ denotes a wave number in the velocity space. Because of the finite resolution, the above simulation scheme works well only when the scale lengths in the phase space are much greater than the grid spacing ($k \ll \pi/\Delta x$ and $\ell \ll \pi/\Delta v$).

By comparing Eqs.(2.29) and (3.7), one will note that Eq.(3.7) is no more than a mapping of f generated by the leap-frog integrator. In other words, f is just advected in the x (v) space by Eq.(3.7) with the velocity v (the acceleration $\partial\phi/\partial x$) which is independent of x (v). Thus, it is straightforward to extend the splitting scheme into higher-orders. A formal solution of Eq.(3.3) is approximated by

$$f^{n+1} = \prod_{i=1}^{k} \exp(-c_i\Delta t D_T)\exp(-d_i\Delta t D_V) f^n + \mathcal{O}(\Delta t^{k+1}) \ . \tag{3.8}$$

Then, the higher-order scheme is given by

$$\prod_{i=1}^{k} \left\{ \begin{array}{l} f^*_{i-1}(q,p) = f_{i-1}(q - c_i\Delta t\ \partial T/\partial p|_{f=f_{i-1}}, p) \\ f_i(q,p) = f^*_{i-1}(q, p + d_i\Delta t\ \partial V/\partial q|_{f=f^*_{i-1}}) \end{array} \right. \ , \tag{3.9}$$

which is a generalization of the splitting scheme.

In order to see accuracy of the higher-order method, we have performed a simulation of the nonlinear Landau damping [9]. The initial condition is given by $f(x, v; t = 0) = F_M(v)(1 - A\cos kx)$, where $A = 0.5$, $k = 0.5$. In a system with length of $L = 2\pi/k$, we set 64 grid points ($\Delta x = L/64$) with the periodic boundary condition. The velocity space of $-v_{\max} \leq v \leq v_{\max}$ with $v_{\max} = 10$ is discretized by grid points with spacing of $\Delta v = v_{\max}/512$. The time integration is carried out by using the 2nd- (leap-frog) and 4th-order symplectic methods with the time step of $\Delta t = 0.125$.

Fluctuations of the total energy in the 2nd- and 4th-order simulations are shown in Fig.3.2. One can see that the energy conservation is largely improved by using the 4th-order integration scheme.

Contour plots of the distribution function in the phase space are shown in Fig.3.3. As we have discussed in the above, fine-scale structures of f in the velocity space become dominant due to the phase mixing. Then, one can see folding of f which shows the particle trapping. Under the physical and numerical parameters given above, the simulation should be stopped at $t = 40$, when the fluctuation scale-length becomes as small as the grid size.

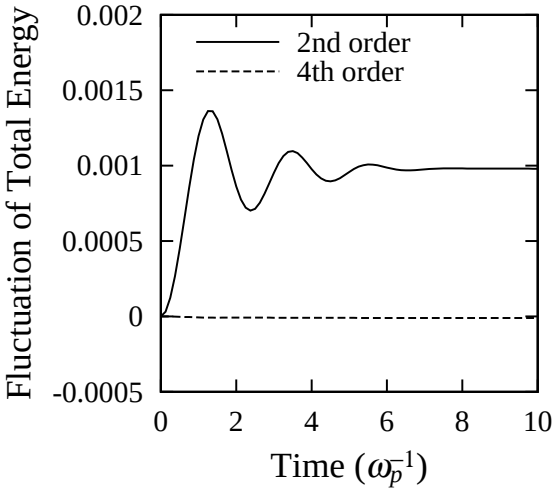

Figure 3.2: Fluctuation of the total energy in simulations of the nonlinear Landau damping. Solid and dashed curves represent results of 2nd and 4th-order schemes, respectively.

3.3 Application to the plasma echo

Here, we try to simulate the temporal plasma echo [10] which is considered to be one of the most difficult problems in simulations of the Vlasov-Poisson system. The initial distribution function is given by the Maxwellian homogeneous in the x-space. The boundary condition in x is periodic. Electrostatic potential of $\Phi\cos k_1 x$ is *externally* added at $t = 0$

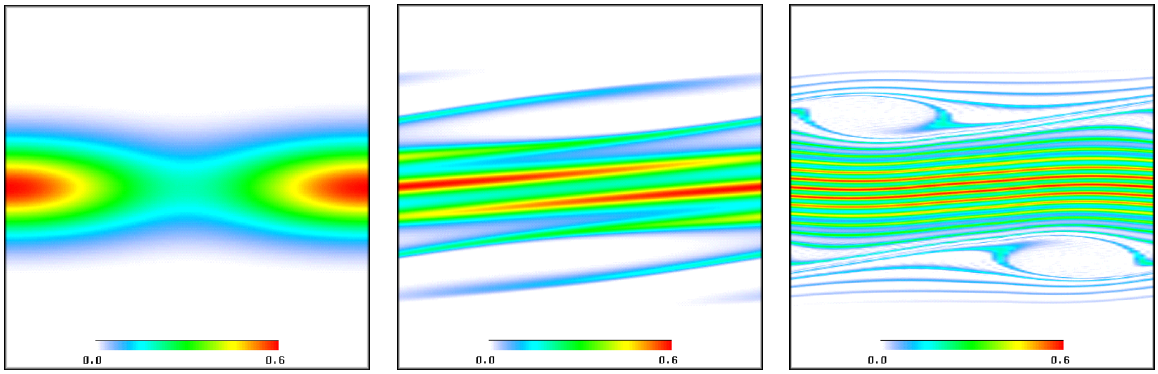

Figure 3.3: Contour maps of the distribution function in the phase space obtained by a simulation of the nonlinear Landau damping at $t = 0$, 10, and $40\omega_{pe}^{-1}$ (from the left to the right).

with a duration time τ_D. The second pulse is given at $t = \tau$ with the wave form of $\Phi \cos k_2 x$ for the same period. We expect a temporal echo appears at $t = t_{\rm echo} = \tau k_2/(k_2 - k_1)$ with the wave number of $k_3 = k_2 - k_1$. In the results shown below, we set $\tau = 30\omega_p^{-1}$, $k_1\lambda_D = \pi$, $k_2\lambda_D = 5\pi/4$, $\Phi = 0.1$ and $\tau_D = 0.125\omega_p^{-1}$. Thus, $t_{\rm echo} = 150\omega_p^{-1}$ and $k_3\lambda_D = \pi/4$.

The x-space with the length of $16\lambda_D$ is discretized by 64 grid points. The velocity space of $-10v_t \leq v \leq 10v_t$ is represented by 4097 grid points. The time step is set to be $\Delta t = \omega_p^{-1}/8$.

A time-evolution of the plasma echo obtained by the Vlasov simulation is shown in Fig.3.4 (left). The appearance time $t_{\rm echo}$ and the wave number k_3 are consistent with the theoretical estimates. In the right panel of Fig.3.4, horizontal axis is magnified for clear plotting, where one can see a non-symmetric profile of the echo [10]. In this simulation, it is essential to employ huge numbers of grid points in the velocity space in order to keep sufficient resolution to the phase mixing process. Otherwise, no clear echo is observed. The obtained result verifies that the phase mixing process with the time-reversibility is successfully reproduced by the Vlasov simulation based on the symplectic integrator.

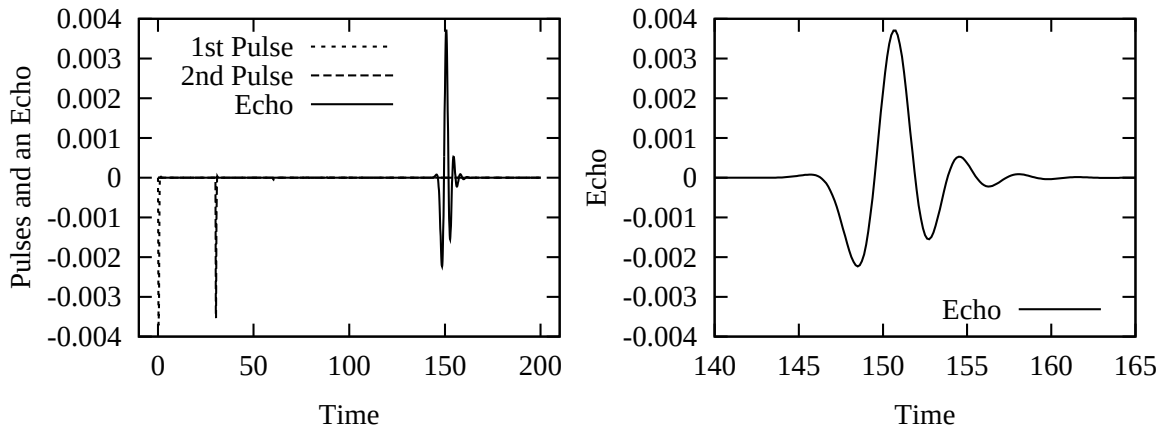

Figure 3.4: Time evolutions of input pulses and an echo (left). A detailed profile of the echo is plotted with magnified horizontal axis (right).

Chapter 4

Numerical simulation of the drift kinetic system

The collisionless electrostatic drift kinetic equation on $f(\boldsymbol{x}, v_\parallel; t)$ in a slab geometry with uniform magnetic field $\boldsymbol{B}$

$$\frac{\partial f}{\partial t} + v_\parallel \nabla_\parallel f + \boldsymbol{v}_{E\times B} \cdot \nabla f + E_\parallel \frac{\partial f}{\partial v_\parallel} = 0 \tag{4.1}$$

(in normalized units) also has the parallel advection term which generates fine-scale structures of f in the velocity space. $v_\parallel$ and $\boldsymbol{v}_{E\times B}$ denote the parallel (to the magnetic field) and the $\boldsymbol{E}\times\boldsymbol{B}$ drift velocities, respectively. $E_\parallel$ means a component of the electric field $\boldsymbol{E}$ parallel to $\boldsymbol{B}$. The gyrokinetic equation also has the same structure as Eq.(4.1). In this chapter, let us consider a simulation scheme suitable for solving Eq.(4.1).

4.1 Time-reversible scheme

In the electrostatic case, $\boldsymbol{E} = -\nabla\phi$, the Hamiltonian of a particle is given by

$$H(x_{\perp 1}, x_{\perp 2}, x_\parallel, v_\parallel) = \frac{1}{2} v_\parallel^2 + \phi(x_{\perp 1}, x_{\perp 2}, x_\parallel) \ . \tag{4.2}$$

Since the $\boldsymbol{E}\times\boldsymbol{B}$ drift motion is represented as

$$\begin{cases} \dot{x}_{\perp 1} = -\partial\phi/\partial x_{\perp 2} \\ \dot{x}_{\perp 2} = \partial\phi/\partial x_{\perp 1} \end{cases} \ , \tag{4.3}$$

$(x_{\perp 1}, x_{\perp 2})$ is a conjugate pair of the coordinates. Then, by using a compact form of the coordinates, $z = (x_{\perp 2}, x_\parallel, x_{\perp 1}, v_\parallel)$, the equation of motion of an $E\times B$ drift particle is written as

$$\dot{z} = \{z, H(z)\} \ . \tag{4.4}$$

Similarly, the drift kinetic equation is rewritten as

$$\frac{\partial f}{\partial t} = -\{f, H\} \ , \tag{4.5}$$

which is the same as Eq.(3.3). In the drift kinetic system (as well as the gyrokinetic system), however, the Hamiltonian $H(z)$ is non-separable for $(x_{\perp 1}, x_{\perp 2})$. Thus, we need to use an implicit symplectic scheme instead of the explicit one that is applied to the Vlasov-Poisson system.

Let us remember the implicit midpoint rule, Eq.(2.33). Applying Eq.(2.33) to the equation of motion of a drift particle, Eq.(4.4), one finds

$$z^{n+1} = z^n + \Delta t \left\{ z, H(\bar{z}) \right\} \quad \text{with} \quad \bar{z} = \frac{z^{n+1} + z^n}{2} \ , \tag{4.6}$$

which generates a mapping of f, such that

$$f^{n+1}(z) = f^n \left[z - \Delta t \left\{ z, H(\bar{z}) \right\} \right] \ . \tag{4.7}$$

From a viewpoint of the numerical scheme, a direct calculation of Eq.(4.7) is difficult, because the splitting technique explained in section 3.2 can not be applied to the non-separable Hamiltonian system.

Instead of the direct calculation of Eq.(4.7), then, it is more straightforward to apply the implicit midpoint rule, Eq.(2.33), to f (not to z), which gives

$$f^{n+1} = f^n - \Delta t \left\{ \bar{f}, \bar{H} \right\} \quad \text{with} \quad \bar{f} = \frac{f^{n+1} + f^n}{2} \ . \tag{4.8}$$

This method apparently preserves the time-reversibility of the drift kinetic equation, Eq.(4.1).

It is important to note that, when the operator $\boldsymbol{F}$ in Eq.(2.33) represents the advection term by an incompressible flow, such that $\boldsymbol{F}(\bar{\boldsymbol{U}}) = -\boldsymbol{V} \cdot \nabla \boldsymbol{U}$ with $\nabla \cdot \boldsymbol{V} = 0$, the implicit midpoint rule exactly satisfies the conservation law of *energy*, $|\boldsymbol{U}|^2$, that is,

$$\left| \boldsymbol{U}^{n+1} \right|^2 + |\boldsymbol{U}^n|^2 = -\Delta t \nabla \cdot \left(\left| \bar{\boldsymbol{U}} \right|^2 \boldsymbol{V} \right) \ . \tag{4.9}$$

Since the Hamiltonian flow is also incompressible in the phase space, Eq.(4.8) leads to

$$\left| f^{n+1} \right|^2 - |f^n|^2 = -\Delta t \left\{ \left| \bar{f} \right|^2, \bar{H} \right\} \ . \tag{4.10}$$

In a system with the periodic boundary for the real space, or, if the surface integrals can be omitted, the integral $\int d^3x dv_\parallel f^2$ (where $f \to 0$ for $v_\parallel \to \pm\infty$) is conserved throughout the numerical time-integration. Therefore, the time-integration method in Eq.(4.8) is nondissipative. This is the advantage in simulations of collisionless kinetic plasmas, while $\int f^m d^6z$ for any integer m as well as $\int f \ln f d^6z$ is also conserved in the real Vlasov and/or drift kinetic systems.

4.2 Application to the ion temperature gradient driven system

4.2.1 Model settings

Here, we consider the drift kinetic equation for the perturbed ion distribution function $\tilde{f}_{\boldsymbol{k}}$ with a wave number $\boldsymbol{k}$ in a two-dimensional slab geometry with the uniform magnetic field in the y-z plane,

$$\begin{aligned} \partial_t \tilde{f}_{\boldsymbol{k}} &+ i\Theta v_\parallel k_y \tilde{f}_{\boldsymbol{k}} + \sum_{\boldsymbol{k}=\boldsymbol{k}'+\boldsymbol{k}''} \left(k'_y k''_x - k'_x k''_y\right) \Psi_{\boldsymbol{k}'} \tilde{f}_{\boldsymbol{k}''} \\ &= -ik_y \Psi_{\boldsymbol{k}} \left[1 + \frac{\eta_i}{2}\left\{v_\parallel^2 - 1 - k^2\right\} + \Theta v_\parallel\right] F_M(v_\parallel) \end{aligned} \tag{4.11}$$

$$\Psi_{\boldsymbol{k}} = e^{-k^2/2}\phi_{\boldsymbol{k}} \ , \tag{4.12}$$

$$\left[1 - \Gamma_0(k^2)\right]\phi_{\boldsymbol{k}} = e^{-k^2/2}\int \tilde{f}_{\boldsymbol{k}}(v_\parallel)dv_\parallel - \tilde{n}_{e,\boldsymbol{k}} \ , \tag{4.13}$$

where $k^2 = k_x^2 + k_y^2$ and $\Gamma_0(k^2) = \exp(-k^2)I_0(k^2)$. $I_0(z)$ denotes the zero-th order modified Bessel function of z. Here, the periodic boundary condition is employed both for the x and y directions. The above set of equation is normalized as follows; $x = x'/\rho_i$, $y = y'/\rho_i$, $v = v'/v_{ti}$, $t = t'v_{ti}/L_n$, $\eta_i = L_n/L_T$, and $\phi = e\phi' L_n/T_i\rho_i$ with the elementary charge e and the background ion temperature T_i ($= m_i v_{ti}^2$; m_i means the ion mass). We have also taken $T_i = T_e$. Parameter η_i is defined by the ratio of scale lengths of background ion density and temperature gradients, L_n and L_t. $\Theta = \theta L_n/\rho_i$ where $\theta = B_y/B_z \ll 1$ and ρ_i is the thermal ion gyroradius. Equations (4.11)-(4.13) are obtained by integrating the gyrokinetic equation [11] for $v_\perp$, assuming $\tilde{f}_{\boldsymbol{k}}(v_\parallel, v_\perp) = \tilde{f}_{\boldsymbol{k}}(v_\parallel)F_M(v_\perp)$ where $k_\perp = \sqrt{k_x^2 + k_y^2}$. The electron response is adiabatic,

$$\tilde{n}_{e,\boldsymbol{k}} = \begin{cases} \phi_{\boldsymbol{k}} & \text{for } k_y \neq 0 \\ 0 & \text{for } k_y = 0 \end{cases} \ . \tag{4.14}$$

The above set of equations describes the ion temperature gradient (ITG) instability driven by the fixed temperature gradient of background ions with the Maxwellian distribution F_M. The same model is also used for simulations of the ITG turbulence which is considered to be a possible mechanism for the anomalous ion heat transport in high-temperature plasmas.

4.2.2 3-mode ITG system

In this subsection, we consider a reduced set of Eq.(4.11) obtained by keeping only $(m, n) = (\pm 1, \pm 1)$ and $(\pm 2, 0)$ modes with the following symmetry conditions of $\tilde{f}_{1,1} = \tilde{f}_{-1,1} = \tilde{f}^*_{1,-1} = \tilde{f}^*_{-1,-1}$ and $\tilde{f}_{2,0} = \tilde{f}^*_{-2,0}$. Here, (m, n) denotes mode numbers in the (x, y)

space. We also assume $\mathrm{Re}(\tilde{f}_{2,0}) = 0$. From Eqs.(4.11) to (4.13), in the long wavelength limit ($k^2 \to 0$, $e^{-k^2/2} \to 1$, and $\Gamma_0 \to 1$), we find the 3-mode ITG system

$$(\partial_t + ik_0\Theta v)f(v,t) + 2ik_0^2\phi(t)h(v,t) = -ik_0\phi(t)G(v) \ , \tag{4.15}$$

$$\partial_t h(v,t) = 4k_0^2 \mathrm{Im}[\phi^*(t)f(v,t)] \ , \tag{4.16}$$

$$\phi(t) = \int dv \ f(v,t) \ , \tag{4.17}$$

where f and ϕ are complex-valued while h is real-valued. Also, we have taken $k_0 = k_x = k_y$. $G(v)$ is defined as

$$G(v) \equiv \left[1 + \frac{\eta_i}{2}(v^2 - 1) + \Theta v\right] F_M(v) \ . \tag{4.18}$$

This problem has often been examined in benchmark tests of many simulation codes for the ITG instability (see references in Ref.[6]).

A class of exact solutions of the nonlinear 3-mode ITG equations is derived in terms of the real and imaginary parts of the linear eigenfunction $f_L(v)$ and the real eigenfrequency ω_r as [6]

$$\begin{aligned} f(v,t) &= [a(t)f_{Lr}(v) + ib(t)f_{Li}(v)]\exp(-i\omega_r t), \\ h(v,t) &= c(t)f_{Li}(v), \\ \phi(t) &= a(t)\exp(-i\omega_r t) \ , \end{aligned} \tag{4.19}$$

where $a(t)$, $b(t)$, and $c(t)$ are real-valued functions of the time t. Here, the linear solution is given by

$$\begin{aligned} f_L(v) &\equiv f_{Lr}(v) + if_{Li}(v) \\ &\equiv \frac{k_0 G(v)}{(\omega_r - k_0\Theta v) + i\gamma} \\ &\equiv \frac{k_0 G(v)[(\omega_r - k_0\Theta v) - i\gamma]}{(\omega_r - k_0\Theta v)^2 + \gamma^2} \ , \end{aligned} \tag{4.20}$$

$$h_L(v) \equiv 0, \qquad \text{and} \qquad \phi_L \equiv 1 \ \ \text{(normalization)} \ , \tag{4.21}$$

The complex eigenfrequency $\omega = \omega_r + i\gamma$ is determined by the dispersion relation

$$\int dv \ f_L(v) \equiv \int dv \frac{k_0 G(v)}{(\omega_r - k_0\Theta v) + i\gamma} = 1 \ , \tag{4.22}$$

where $\gamma > 0$ is assumed.

Substituting these into Eqs.(4.15)–(4.17) and using Eq.(4.20), we obtain the ordinary differential equations for $[a(t), b(t), c(t)]$,

$$\begin{aligned} da/dt &= \gamma b \ , \\ db/dt &= \gamma a - 2k_0^2 ac \ , \\ dc/dt &= 4k_0^2 ab, \end{aligned} \tag{4.23}$$

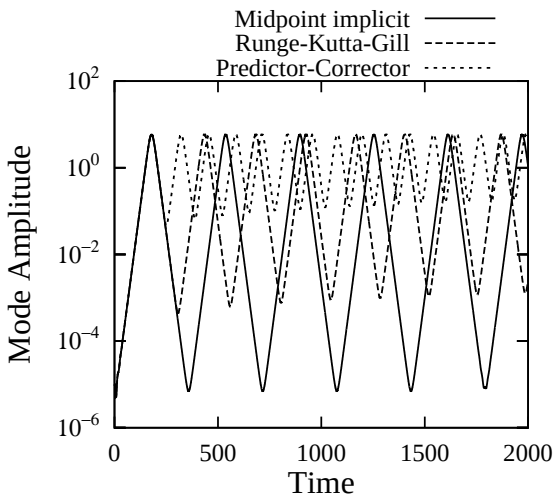

Figure 4.1: Comparison of the implicit midpoint scheme with the predictor-corrector and the Runge-Kutta-Gill methods for $k_0 = 0.1$, $\eta_i = 10$, $\Theta = 1$, and $\varepsilon = 10^{-5}$ [9].

which is equivalent to Eq.(2.38) discussed in section 2.4. Then, its solution is given by the Jacobi elliptic functions and is periodic in time.

Numerical simulations of the 3-mode ITG system given by Eqs.(4.15)-(4.17) are carried out by means of three different time-integrations schemes. Let us compare the simulation results with each other, where the implicit midpoint rule in Eq.(4.8), the predictor-corrector, and the Runge-Kutta-Gill methods are used. The last two methods are second and fourth-order explicit schemes, respectively. The predictor-corrector method used here is written as [12]

$$\begin{cases} \boldsymbol{U}^* = \boldsymbol{U}^{n-1} + 2\Delta t \boldsymbol{F}(\boldsymbol{U}^n) \\ \boldsymbol{U}^{n+1} = \boldsymbol{U}^n + \Delta t \boldsymbol{F}\left[(\boldsymbol{U}^* + \boldsymbol{U}^n)/2\right] \ , \end{cases} \tag{4.24}$$

which is known to be weakly dissipative.

The initial condition is given by $f_\pm(v, t = 0) = \varepsilon F_M(v)$ and $f_2(v, t = 0) = 0$. The velocity space of $-5v_t \leq v \leq 5v_t$ is represented by 129 grid points. The time step is $\Delta t = 0.25$. Figure 4.1 shows the simulation results for $k_0 = 0.1$, $\eta_i = 10$, $\Theta = 1$, and $\varepsilon = 10^{-5}$. For these parameters, the analytical solution predicts the period of $T = 353$. With respect to the linear growth rate and the first peak level of $|\phi|$, the three methods give the same results. After the peaking, $|\phi|$ decreases with the same rate as in the linear growth phase. The nondissipative simulation with the implicit midpoint rule in Eq.(4.8) (as well as its fourth-order version) can accurately reproduce the analytical solution of the 3-mode ITG equation. In the case of the predictor-corrector method, however, the exponential decay stops at $|\phi| = 4.63 \times 10^{-2}$ due to the numerical dissipation, and then, the mode grows again. The periodic behavior of $|\phi|$ is lost by the predictor-corrector scheme. Thus, time interval of the first and second peaks of $|\phi|$ is shorter ($T = 143$) than a half of the period given by the analytical solution. Although the fourth-order Runge-

Kutta-Gill method is less dissipative than the predictor-corrector, the periodic solution is not correctly reproduced. The minimum value of $|\phi|$ is 4.45×10^{-4}, and the interval of the first and second peaks is $T = 256$. The above comparison with the dissipative integrators highlights the success of the nondissipative scheme in Eq.(4.8).

4.2.3 Drift wave echo

In order to verify the accuracy of the nondissipative scheme in Eq.(4.8) for the phase mixing process, let us consider a temporal plasma echo in the drift kinetic system. The simulation model is the same as that described in section 4.2.1. The initial perturbed distribution function is set to be zero. We also assume the symmetry of $f_{k_x,k_y} = f_{-k_x,k_y}$. Electrostatic potential of $\Phi \cos k_1 x \cos k_1 y$ is *externally* added at $t = 0$ with a duration time τ_D. The second pulse is given at $t = \tau$ with the wave form of $\Phi \cos k_2 x \cos k_2 y$ for the same period. We expect that a temporal echo appears at $t = t_{\rm echo} = \tau k_2/(k_2 - k_1)$ with the wave number of $k_{3,x} = k_1 + k_2$ and $k_{3,y} = k_2 - k_1$ (the ion diamagnetic drift is in the $-y$-direction). We choose parameters of $\eta_i = 0$ and $\Theta = 1$. In the results shown below, we set $\tau = 30 L_n/v_t$, $k_1\rho_i = 0.4$, $k_2\rho_i = 0.5$, $\Phi = 0.1$ and $\tau_D = 0.2 L_n/v_t$. Thus, $t_{\rm echo} = 150 L_n/v_t$, $k_{3,x}\rho_i = 0.9$, and $k_{3,y}\rho_i = 0.1$.

The minimum and maximum wave numbers are, respectively, $0.1\rho_i^{-1}$ and $1.0\rho_i^{-1}$ with the 3/2-rule for de-aliasing. The velocity space of $-5v_t \le v_\parallel \le 5v_t$ is represented by 2049 grid points. The recurrence time is estimated as $t_r \equiv 2\pi/k\Delta v_\parallel = 2048\pi/5 \sim 1286 L_n/v_t$ which is much longer than the simulation time. Then, we have enough resolution for the velocity space. The time step is set to be $\Delta t = 0.1 L_n/v_t$.

Time history of $(k_x, k_y) = (k_1 + k_2, k_2 - k_1)$ mode is shown in Fig.4.2. The appearance time of the echo $t_{\rm echo}$ and the wave numbers $k_{3,x}$ and $k_{3,y}$ agree with the theoretical estimates. The obtained result shows that the phase mixing process with the time-reversibility is successfully reproduced by the simulation with the nondissipative time integration scheme.

4.2.4 Remarks on ITG turbulence simulation

Eqs.(4.11)-(4.13) are also employed for simulations of the ITG turbulent transport [6]. The nondissipative simulation method based on the implicit midpoint rule, Eq.(4.8), has a benefit of preserving the entropy balance.

By multiplying $\tilde{f}^*_{\boldsymbol{k}}/F_M$ to Eq.(4.11), and using Eqs.(4.12) and (4.13), we find

$$\frac{d}{dt}\left(\delta S + W\right) = \eta_i Q_i \ , \tag{4.25}$$

where $\delta S \equiv \sum_{\boldsymbol{k}} \int dv_\parallel |\tilde{f}_{\boldsymbol{k}}|^2/2F_M$; the potential energy W is defined as $W = \sum_{\boldsymbol{k}}[1 - \delta_{k_y,0} + (T_e/T_i)(1 - \Gamma_0)]|\phi_{\boldsymbol{k}}|^2/2$. The perpendicular ion thermal transport flux Q_i is $Q_i = \sum_{\boldsymbol{k}} \int dv_\parallel (-ik_y e^{-k^2/2}\phi_{\boldsymbol{k}}) v_\parallel^2 \tilde{f}_{-\boldsymbol{k}}/2$. Also, δS is rewritten as $\delta S = S_{\rm M} - S_{\rm m}$ where $S_{\rm M} = -\int d^3v F_M \ln F_M$ and $S_{\rm m} = -\langle \int d^3v f \ln f \rangle$, with $f = F_M + \delta f$, represent macroscopic and microscopic entropy per unit volume, respectively. $\langle \cdots \rangle$ denotes the ensemble average.

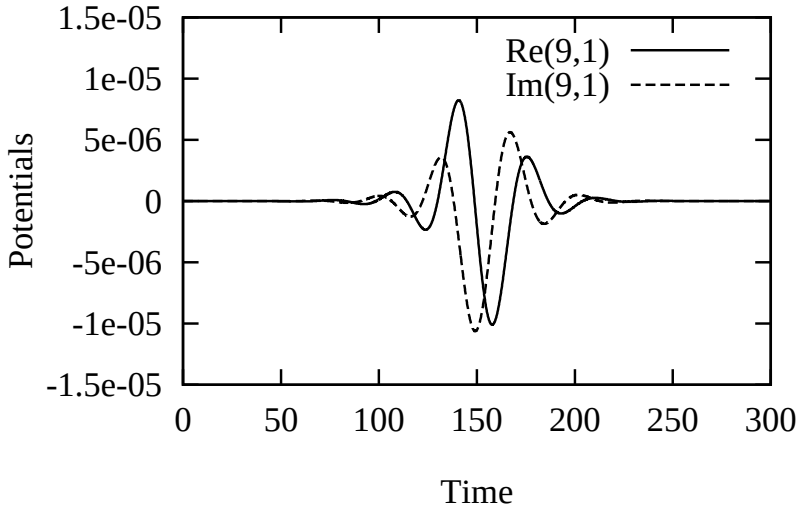

Figure 4.2: Drift wave echo found in potential evolution of (k_1+k_2, k_2-k_1) mode of which amplitude peaks at $t = 150L_n/v_t$ as is expected by the theoretical estimate.

The entropy variable δS is the opposite sign of the excess entropy defined by Glansdorff and Prigogine [13]. Thus, Eq.(4.25) is called the *entropy* balance equation.

As is seen in Eq.(4.10), the nondissipative scheme guarantees conservation of δS. Therefore, by using the simulation scheme given in Eq.(4.8), the entropy balance equation can be accurately calculated. It should be noted that the entropy production rate $d(\delta S)/dt$ balances with $\eta_i Q_i$ if a constant transport flux Q_i is observed in a steady turbulent flow $(dW/dt = 0)$. This means that precise evaluation of δS is a key to understand a mechanism of the collisionless plasma turbulent transport. Results of the nondissipative simulation of the ITG turbulence are found in Ref.[14].

Chapter 5

Kinetic fluid simulations models

In this chapter, let us consider kinetic-fluid simulation models which are designed with the aim of reproducing behaviors of low-order velocity-space moments of f in terms of fluid variables such as density, momentum, temperature, *etc.*

5.1 Closure models

By taking 0th to 2nd order velocity-space moments of Eq.(4.11) in the long wavelength limit ($k^2 \to 0$, $e^{-k^2/2} \to 1$, and $\Gamma_0 \to 1$), we find the following set of fluid equations,

$$\partial_t n_{\boldsymbol{k}} + ik_\parallel u_{\boldsymbol{k}} - i\boldsymbol{k}_\perp \cdot \hat{\boldsymbol{b}} \times \hat{\boldsymbol{n}} \phi_{\boldsymbol{k}} - \sum_{\boldsymbol{k}=\boldsymbol{k}'+\boldsymbol{k}''} \hat{\boldsymbol{b}} \cdot \boldsymbol{k}' \times \boldsymbol{k}'' \phi_{\boldsymbol{k}'} n_{\boldsymbol{k}''} = 0 \ , \tag{5.1}$$

$$\partial_t u_{\boldsymbol{k}} + ik_\parallel (n_{\boldsymbol{k}} + T_{\boldsymbol{k}} + \phi_{\boldsymbol{k}}) - \sum_{\boldsymbol{k}=\boldsymbol{k}'+\boldsymbol{k}''} \hat{\boldsymbol{b}} \cdot \boldsymbol{k}' \times \boldsymbol{k}'' \phi_{\boldsymbol{k}'} u_{\boldsymbol{k}''} = 0 \ , \tag{5.2}$$

$$\partial_t T_{\boldsymbol{k}} + ik_\parallel (2u_{\boldsymbol{k}} + q_{\boldsymbol{k}}) - i\eta_i \boldsymbol{k}_\perp \cdot \hat{\boldsymbol{b}} \times \hat{\boldsymbol{n}} \phi_{\boldsymbol{k}} - \sum_{\boldsymbol{k}=\boldsymbol{k}'+\boldsymbol{k}''} \hat{\boldsymbol{b}} \cdot \boldsymbol{k}' \times \boldsymbol{k}'' \phi_{\boldsymbol{k}'} T_{\boldsymbol{k}''} = 0 \ , \tag{5.3}$$

where $n_{\boldsymbol{k}} = \int dv_\parallel \tilde{f}_{\boldsymbol{k}}$, $u_{\boldsymbol{k}} = \int dv_\parallel \tilde{f}_{\boldsymbol{k}} v_\parallel$, $T_{\boldsymbol{k}} = \int dv_\parallel \tilde{f}_{\boldsymbol{k}} (v_\parallel^2 - 1)$, and $q_{\boldsymbol{k}} = \int dv_\parallel \tilde{f}_{\boldsymbol{k}} (v_\parallel^3 - 3v_\parallel)$. $\hat{\boldsymbol{b}}$ and $\hat{\boldsymbol{n}}$ denote unit vectors in directions of the magnetic field and the density gradient, respectively. Here, the quasi-neutrality condition with the adiabatic electron response is given by $n_{\boldsymbol{k}} = \phi_{\boldsymbol{k}}$ without considering the exceptional treatment for the zonal flow components with $k_y = 0$. Since the parallel heat flux $q_{\boldsymbol{k}}$ appears in Eq.(5.3), in order to close the fluid equations, one needs a closure model which represents $q_{\boldsymbol{k}}$ in terms of lower-order moments, $n_{\boldsymbol{k}}$, $u_{\boldsymbol{k}}$, and $T_{\boldsymbol{k}}$. This is called the closure problem.

It is an important subject in kinetic-fluid simulations of turbulent transport what kind of closure model should be employed. From Eqs.(5.1) to (5.3), one finds the entropy balance equation in the kinetic-fluid system,

$$\frac{d}{dt} \sum_{\boldsymbol{k}} \left(\frac{|n_{\boldsymbol{k}}|^2}{2} + \frac{|u_{\boldsymbol{k}}|^2}{2} + \frac{|T_{\boldsymbol{k}}|^2}{2} \right) + \frac{dW}{dt} = \eta_i Q_i + \sum_{\boldsymbol{k}} \mathrm{Re} \left(\frac{ik_\parallel}{2} T_{\boldsymbol{k}} q_{\boldsymbol{k}}^* \right) \ , \tag{5.4}$$

which corresponds to Eq.(4.25) in the long wavelength limit. Since the left hand side of Eq.(5.4) vanishes in a steady state, the transport flux Q_i balances with a correlation term between $T_{\boldsymbol{k}}$ and $q^*_{\boldsymbol{k}}$ which depends on the closure model itself.

Hammett and Perkins (H-P) proposed a simple kinetic-fluid closure model [15], that is,

$$q_{\boldsymbol{k}} = -i\sqrt{\frac{8}{\pi}}\frac{k_\parallel}{\left|k_\parallel\right|}T_{\boldsymbol{k}} \ , \tag{5.5}$$

which can reproduce the linear Landau damping as well as the linear dispersion relation of the slab ITG mode. One finds that the H-P closure model brings the dissipation (irreversibility) into Eq.(5.3), while the kinetic equation is nondissipative with the time-reversal symmetry.

Contrary to the H-P closure model, a nondissipative closure model (NCM) for linearly unstable modes is also considered [16], such that,

$$q_{\boldsymbol{k}} = C_{T\boldsymbol{k}}T_{\boldsymbol{k}} + C_{u\boldsymbol{k}}u_{\boldsymbol{k}} \ , \tag{5.6}$$

with real-valued coefficients, $C_{T\boldsymbol{k}}$ and $C_{u\boldsymbol{k}}$, which are determined so as to reproduce the linear dispersion relation of the ITG mode. Thus, the time-reversibility of the unstable modes can be preserved even in the kinetic-fluid system.

5.2 Application to the 3-mode ITG system

In order to see effects of the closure models, let us consider the 3-mode ITG problem in the set of kinetic-fluid equations. The model setting is the same as that in section 4.2.2. Then, one finds the same set of O.D.E.'s as Eq.(4.23). The implicit midpoint rule is employed for the time-integration. Results of the numerical simulations with three different closure models are shown in Fig.5.1, where the potential amplitude of $(1,1)$ mode is plotted for the H-P closure, NCM, and the adiabatic closure model of $q_{\boldsymbol{k}} = 0$. The NCM result exactly agrees with the analytical solution given by the Jacobi elliptic function. The potential amplitude in the H-P model is, however, saturated at a certain constant amplitude, while a periodic behavior of the solution is also preserved even with the adiabatic model of $q_{\boldsymbol{k}} = 0$. The qualitative difference found in simulations of the H-P closure and the other two models is due to the breaking of the time-reversibility introduced by Eq.(5.5). The obtained result demonstrates that keeping the time-reversibility is essential to the test nonlinear problem of the 3-mode ITG system. For comparison between the kinetic and fluid simulations of the ITG turbulence, one may refer to a recent work given in Ref.[17].

In summary, preserving the time-reversibility is important in considering the kinetic-fluid closure model. As seen in previous chapters, one also needs to take care of the time-reversibility of the numerical time-integration scheme employed in the kinetic-fluid simulation. Otherwise, all efforts to construct the closure model may come to nothing.

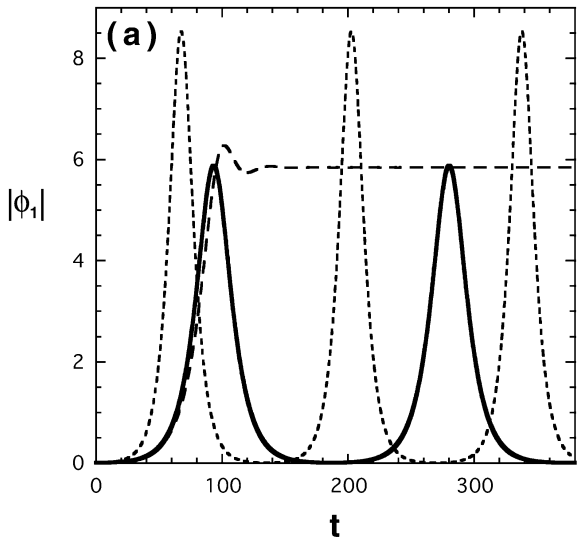

Figure 5.1: Numerical solution of the 3-mode ITG problem in kinetic-fluid models. Time-evolutions of the potential amplitude given by the H-P closure (dashed), NCM (solid), and the adiabatic closure model of $q_{\boldsymbol{k}} = 0$ (dotted) are plotted as functions of the time t [16].

Bibliography

[1] H.Goldstein, *"Classical Mechanics"* (2nd Ed., Addison-Wesley, Reading, Massachusetts, 1980).

[2] H.Yoshida, Phys.Lett. **150**, 162 (1990).

[3] C.K.Birdsall and A.B.Langdon, *"Plasma Physics via Computer Simulation"* (McGraw-Hill, New York, 1985).

[4] E.Forest, and R.D.Ruth, Physica D **43**, 105 (1990).

[5] J.M.Sanz-Serna, Physica D **60**, 293 (1992).

[6] T.-H.Watanabe, H.Sugama, and T.Sato, Phys.Plasmas **7**, 984 (2000).

[7] C.Z.Cheng and G.Knorr, J.Comput.Phys. **22**, 330 (1976).

[8] M.Shoucri and R.Gagné, J.Comput.Phys. bf 27, 315 (1978).

[9] T.-H.Watanabe, H.Sugama, and T.Sato, J.Phys.Soc.Jpn **70**, 3565 (2001).

[10] S.Ichimaru, "*Statistical Plasma Physics Vol.I: Basic Principles*" (Addison-Wesley, Redwood City, 1992) Chap.5 and references therein.

[11] D.H.E.Dubin, J.A.Krommes, C.Oberman, and W.W.Lee, Phys. Fluids **26**, 3524 (1983).

[12] W.W.Lee and H.Okuda, J.Compt.Phys. **26**, 139 (1978).

[13] P.Glansdorff, and I.Prigogine, "*Thermodynamic Theory of Structure, Stability and Fluctuations*" (Wiley-Interscience, London, 1971).

[14] T.-H.Watanabe and H.Sugama, Phys.Plasmas **9**, 3659 (2002).

[15] G.W.Hammett and F.W.Perkins, Phys.Rev.Lett. **64**, 3019 (1990).

[16] H.Sugama, T.-H.Watanabe, and W.Horton, Phys.Plasmas **8**, 2617 (2001).

[17] H.Sugama, T.-H.Watanabe, and W.Horton, Phys.Plasmas **10**, 726 (2003).